PCCP

Bonding of C1 Fragments on Metal Nanoclusters: A Search for Methane Conversion Catalysts with Swarm Intelligence

Journal:	*Physical Chemistry Chemical Physics*
Manuscript ID	CP-ART-01-2021-000345.R3
Article Type:	Paper
Date Submitted by the Author:	19-May-2021
Complete List of Authors:	Hori, Mikiya; Kyushu University, Institute for Materials Chemistry and Engineering Tsuji, Yuta; Kyushu University, Institute for Materials Chemistry and Engineering Yoshizawa, Kazunari; Kyushu University, Institute for Materials Chemistry and Engineering

SCHOLARONE™
Manuscripts

ARTICLE

Bonding of C_1 Fragments on Metal Nanoclusters: A Search for Methane Conversion Catalysts with Swarm Intelligence†

Received 00th January 20xx,
Accepted 00th January 20xx

DOI: 10.1039/x0xx00000x

Mikiya Hori,[a] Yuta Tsuji*[a] and Kazunari Yoshizawa*[a]

There is a need for a catalyst that can directly convert methane into useful substances. The use of Ni as a catalyst for the steam reforming of methane has led us to look at Ni nanoclusters as potential candidates for the direct conversion of methane. Fe, Co, Cu, and Zn nanoclusters are also focused on. How the type of C_1 fragments (CH_4, CH_3, CH_2, CH, and C) stabilized by the metal nanoclusters as adsorbed species varies with metal species is theoretically investigated. The particle swarm optimization algorithm, which is based on swarm intelligence, as well as density functional theory is used for this calculation. The Ni nanoclusters are found to preferentially adsorb C as a stable species, the Fe and the Co nanoclusters both CH and CH_3, and the Cu nanoclusters CH_3; the Zn nanoclusters are found not to chemisorb any C_1 fragment. The methane activation capacity can be ranked as the order of Ni > Fe > Co > Cu > Zn. The highest methane activation capacity of Ni is due to the strongest covalent nature of the interaction between Ni and the adsorbed species. The ionicity of the bond between Fe and the adsorbed species is higher than that between Co and the adsorbed species, while the covalent nature of the bonds is comparable for both. The weak methane activation ability of Cu compared to Fe, Co, and Ni is found to be due to the fact that both the covalent and ionic bond strengths between Cu and the adsorbed species are weak. Zn and the adsorbed species form neither ionic nor covalent bond. These results indicate that the Fe and the Co nanoclusters as well as the Ni may lead to the over-oxidation of methane, whereas the Zn nanoclusters cannot activate methane in the first place; therefore, their application to direct methane conversion catalysts is unlikely. Since the Cu nanoclusters do not adsorb C and CH as stable species, but CH_3 stably, the Cu nanoclusters are expected to work as a catalyst for the direct conversion of methane.

I. Introduction

Methane, the main component of natural gas, is converted into syngas, a mixture of hydrogen and carbon monoxide, through steam reforming, and then converted into various useful substances, such as higher hydrocarbons and alcohols.[1-4] Ni is usually used as a catalyst for steam reforming.[5,6] One of the problems with steam reforming is that the reaction takes place under high temperature and pressure conditions of about 900 °C and 20 atm, making the process expensive.[7]

The inefficient reaction pathway of converting methane once into syngas and then into such a target substance as methanol can also be assigned as a cause of the high cost.[8,9] Another problem with the Ni catalyst is that the activity of the catalyst can be reduced due to carbon deposition when the catalyst is used for a long period of time.[10-13] Therefore, there is a need for a catalyst that can directly convert methane into a target material under milder conditions exothermically and that can be used for a long period of time.[14]

The C-H bond in methane has a very large bond dissociation energy of about 4.5 eV (104 kcal/mol),[15] so it would take a lot of energy to cleave it in the gas phase without using a catalyst (see section 1 in ESI† for more details), but this is not the case on the catalyst surface.

An energy diagram of the C-H bond cleavage process of methane on the surface of Ni (111) is shown in Fig. 1.[16] The reason why steam reforming with Ni is performed under high temperature and pressure conditions is because of the high activation energy of the conversion of CH_4 to CH_3*, where * denotes the adsorbed species. Once one C-H bond in methane is broken, methane is easily over-oxidized to CH* because the activation energies for the subsequent dehydrogenation reactions are lower.

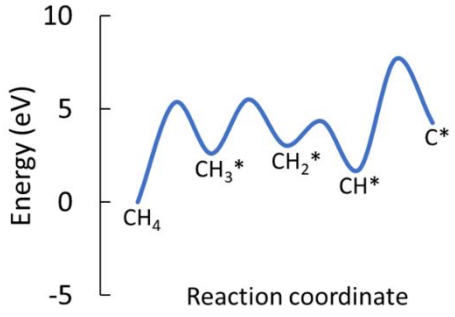

Fig. 1 Energy diagram for the C-H bond cleavage of methane on the Ni (111) surface, generated on the basis of a reference.[16]

[a] *Institute for Materials Chemistry and Engineering and IRCCS, Kyushu University, Nishi-ku, Fukuoka 819-0395, Japan.*
E-mail: yuta@ms.ifoc.kyushu-u.ac.jp, kazunari@ms.ifoc.kyushu-u.ac.jp

†Electronic supplementary information (ESI) available: Energy diagram for the dehydrogenation reaction of CH_4 to C, effects of dipole correction, Boltzmann distribution at 300 K, all cluster structures optimized in this study, magnetic moments of the clusters, radial distribution function for the M-C bonds, entropic effects, interaction of the band of metal with an adsorbate level, DOS plots for the metal nanoclusters and the adsorbed species of CH_3 and H, and atomic coordinates of the optimized structures.

If one succeeds in stabilizing CH_3* and/or CH_2* on a surface, useful compounds, such as ethane and ethylene, are expected to be generated directly from them.[17-22] Therefore, a low activation energy for the conversion of CH_4 to CH_3* and the more stable presence of CH_3* and/or CH_2* than CH* and C* are two necessary conditions for an ideal methane-conversion catalyst.[17]

There has been a wide range of research on methane activation in the literature. The dehydrogenation of methane on the surfaces of Co and Cu, was theoretically studied: Hao et al. reported their thermodynamic and kinetic results of CH_4 dissociation on different Co surfaces, demonstrating that CH_4 dissociation on the Co (100) surface is thermodynamically and kinetically preferable compared to that on the Co (111) and Co (110) surfaces.[23] Gajewski and Pao found that the Cu (111) surface can catalyse the reaction of $CH_4(g) \rightarrow C^* + 4H^*$ by extracting electron density from the C-H bond and simultaneously forming a covalent bond between the C and Cu atoms to stabilize the transition state.[24] Niu et al. theoretically evaluated the catalytic ability for the dehydrogenation of methane on Ni surfaces doped with Pt, finding that doping Ni with Pt increases the activation energy for CH to C dehydrogenation, which reduces the possibility of coke formation.[25] By changing the Miller index of the Ni surface interacting with methane from (111) to (211) as demonstrated in Bengaard et al.'s study,[26] or by changing the Ni surface from a flat one to a stepped one as demonstrated in Arevalo et al.'s study,[27] one can change the ease with which the methane dehydrogenation reaction proceeds. In these previous studies, it can be seen that by changing the structure and composition of the active site interacting with methane, the ease with which the methane dehydrogenation reaction proceeds can be changed.

In recent years, research on catalysts based on metal nanoclusters has been very active.[28-33] The electronic structure of metal nanoclusters is often different from that of solids, and the activity and selectivity for many reactions vary greatly depending on the number of metal atoms that make up the cluster.[34]

Many theoretical studies regarding cluster catalysts for methane activation and conversion have been conducted so far. Seenivasan and Tiwari carried out a computational study using density functional theory (DFT) on Ni_6, Ni_{13}, and Ni_{19} nanoclusters to understand the effect of the size of the nickel nanoclusters on the initial C-H bond dissociation of methane, concluding that the use of the nanoclusters dramatically lowers the activation barrier and that the reactivity is strongly dependent on the size.[35] In our previous study using DFT+U, we revealed that the initial C-H bond cleavage of methane on a Ni_4 cluster supported on the CeO_2 (111) surface takes place via a nonradical route.[36] Cheng et al. investigated the ease of progress of dehydrogenation of methane to carbon on Pt_{21} (hemispherical) and Pt_{20} (tetrahedral) clusters using DFT;[37] They also investigated using DFT+U how the ease of the C-H bond breaking reaction varies when these clusters are loaded either on the CeO_2 (100) surface or on a silica surface.[38] Damte et al. reported a DFT study on the conversion of methane into ethane and ethylene with Ir_4 and Pt_4 cluster catalysts supported on B- and N-doped graphene.[39] Khan et al. presented a report on a theoretical study about methane dehydrogenation and ethylene formation by C-C coupling on Mo_4C_2 and Mo_2C_4 clusters.[40] Collision induced dissociation of methane on small Cu clusters was theoretically investigated by Varghese and Mushrifthe.[41]

Some interesting experimental studies have also been conducted. Wei and Iglesia conducted kinetic measurements of the reactivity of supported noble metal clusters (Rh, Ir, Pt, and Ru) for their catalytic reactions of CH_4, providing a direct comparison of the reactivity of the noble metal clusters at conditions relevant to industrial practice.[42,43] Li et al. demonstrated the conversion of methane to methanol under mild conditions using gold nanoparticles supported on SiO_2.[44] Hou et al. demonstrated that Rh nanoclusters can be formed in zeolites, acting as a catalyst for the partial oxidation of methane to syngas at low temperatures.[45]

While a lot of theoretical studies have been done, several experimental studies have been done as well. However, all of those studies are mostly about metal nanoclusters of a certain number of metal atoms or a certain metal element. Therefore, with the direct conversion of methane by C-C coupling in mind, we have used DFT calculations powered by swarm intelligence to systematically test whether CH_3 can exist as the stable adsorbed species on metal nanoclusters of various metal elements and numbers of metal atoms. This is what is new in this research. We focus not only on Ni nanoclusters but also on Fe, Co, Cu, and Zn nanoclusters.

Metal nanoclusters take on a variety of structures. Unlike metal surfaces, they have a variety of active sites that can interact with methane. Therefore, it would take an enormous amount of time to analyse the interaction of each active site of every metal nanocluster with methane one by one. In order to search for the most stable structure and metastable structures generated upon the adsorption of a C_1 fragment on metal nanoclusters, we make good use of the crystal structure analysis by particle swarm optimization (CALYPSO) program,[46-48] which uses the particle swarm optimization (PSO) algorithm[49-51] for global optimization, together with the DFT program of Vienna ab initio simulation package (VASP)[52-55] for local optimization.

The PSO method is a type of swarm intelligence.[56] In this method, the optimization problem can be solved efficiently by using an algorithm in which the information about energy, searching history, and the position of multiple individuals in the search space is shared with each other in a swarm during the search.[57] In fact, up to this point, many theoretical studies on clusters have been done using CALYPSO to generate stable structures of Pt-Pd alloy clusters,[58] Mg clusters,[59] and Na clusters.[60] This study will provide a basis for the application of the PSO method to catalytic chemistry.

II. Computational Methods

The most stable structure and metastable structures of nanoclusters consisting of one C, four H, and *n* M (M = Fe, Co, Ni, Cu, or Zn; *n* = 1-10) atoms were explored. For this purpose, CALYPSO was used. We used VASP to optimize structures at the DFT level during the search. VASP can only optimize structures on which periodic boundary conditions are imposed. Since nanoclusters are not a periodic system, the calculations were performed by placing a nanocluster in a large orthorhombic unit cell with it surrounded by a vacuum layer. The separations between the nanocluster and its nearest-neighbouring periodic images were set to be longer than 15 Å (see Fig. 2). Note that it has been reported that a calculation in which a molecule is placed in a periodic cell with a vacuum layer and that of the same molecule isolated with no periodic boundary

This journal is © The Royal Society of Chemistry 20xx

Please do not adjust margins

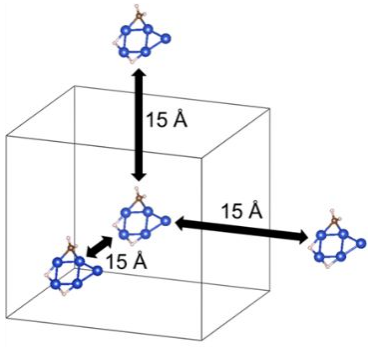

Fig. 2 Example of a unit cell with the most stable Cu_5CH_4 structure. The separations between the optimized cluster and its nearest-neighbouring periodic images are set to longer than 15 Å.

condition imposed give almost consistent results.[61] Zhao, Du, and Jiang[62] calculated transition metal clusters in periodic unit cells including vacuum space, confirming that their results are in good agreement with experimental values. In this study, we used almost the same method as they did. Comparing the metal-to-metal distances in the diatomic clusters optimized by our method with those calculated using the Gaussian program in the literature,[63] we found that the deviation is at most 0.03 Å. This ensures the reliability of our calculations. For molecular calculations with such finite size unit cells, it may be better to consider the effect of dipole corrections. However, as shown in section 2 of ESI†, such an effect was found not to be so significant. Thus, we did not apply it in this study to save computational cost. The molecular structure drawing program of VESTA[64] was used to visualize nanocluster structures.

For comparison, we also used CALYPSO to decide the geometry of each M_n structure by exploring the most stable structure in a system with only n M atoms in the unit cell. However, for systems containing only one or two M atoms, we did not bother to optimize them using CALYPSO because of the lack of structural diversity. The generalized gradient approximation of Perdew, Burke, and Ernzerhof (GGA-PBE)[65] was used as the exchange correlation potential. The calculation conditions for structural optimization were set so that the cutoff energy was 400 eV and the k-point sampling was performed only at the Γ point. The projector augmented wave (PAW) method was used for the pseudopotential.[66,67] The convergence condition for the self-consistent field (SCF) loop was set to 1.0×10^{-4} eV and the convergence condition for structural optimization was set to 1.0×10^{-3} eV. Grimme's DFT-D2 method was used as a dispersion correction.[68] The calculations were performed taking collinear spin polarization into account. The magnetic moments of the optimized cluster structures are tabulated in section 5 of ESI†. Those of the diatomic clusters are consistent with the spin multiplicities of the ground-state transition metal dimers in the literature.[63] Following a study by Szécsényi et al.,[69] we have investigated different spin multiplicities for all the clusters to find their ground state multiplicities. The results are presented in section 5 of ESI†, showing that the spin state predicted using the spin polarization calculation implemented in VASP is correct in almost all the cases. Only for Fe_8, Fe_5CH_4, and $Fe_{10}CH_4$ clusters, VASP failed to predict the correct spin state, so we recalculated them with the correct spin multiplicity.

The local PSO algorithm[70] was adopted to facilitate the search for metastable structures. When generating a new group (next generation) in the PSO calculation, the number of structures per generation (population) was set to 20, where 80% of the 20 were generated by using the local PSO algorithm and the remaining 20% were generated randomly. When there is no update of the most stable structure over more than 10 generations, the PSO calculation using CALYPSO is assumed to have converged. Of the various structures output from CALYPSO, only those with an energy difference of less than 0.1 eV measured from the energy of the most stable structure are considered in this paper. This is because according to the Boltzmann distribution calculated at 300 K (see Fig. S2 in ESI†), the probability of the existence of a structure with an energy higher than the energy of the most stable structure by > 0.1 eV is very small (less than 0.021).

In order to optimize a very large number of structures in the structure search using CALYPSO, the structural optimization with VASP was performed under relatively loose conditions as described earlier. In order to calculate and understand the detailed electronic structures of the obtained most stable and metastable structures, we again performed additional structural optimizations of these structures under more accurate conditions: The convergence condition for SCF was changed to 1.0×10^{-5} eV, the convergence condition for structural optimization was changed to 1.0×10^{-4} eV, and the cutoff energy was set to 500 eV. The other calculation conditions were the same as those used in the structure search.

The Fermi level, vacuum level, and density of states (DOS) were calculated for unit cells containing the most stable metal nanoclusters without any C_1 fragment. Bader charges[71] and the value of the integrated crystal orbital Hamilton population (ICOHP)[72,73] for a pair of atoms were calculated for structures in which a C_1 fragment is adsorbed on a metal nanocluster. LOBSTER[74,75] was used for the ICOHP calculation.

III. Results and Discussion

a. The Most Stable and Metastable Nanocluster Structures Obtained from CALYPSO Structural Search

	Fe	Co	Ni	Cu	Zn
C	Fe_9, Fe_{10}	Co_4, Co_5, Co_{10}	Ni_3, Ni_4, Ni_5, Ni_6, Ni_7, Ni_8, Ni_9, Ni_{10}	—	—
CH	Fe_4, Fe_5, Fe_6, Fe_7, Fe_8, Fe_9, Fe_{10}	Co_3, Co_7, Co_8, Co_{10}	Ni_3	—	—
CH_2	Fe_3, Fe_4	Co_3	Ni_2, Ni_3	Cu_5	—
CH_3	Fe_1, Fe_2, Fe_4, Fe_8	Co_1, Co_2, Co_3, Co_4, Co_6, Co_9	Ni_1, Ni_2, Ni_3	Cu_3, Cu_4, Cu_5, Cu_6, Cu_7, Cu_8, Cu_9, Cu_{10}	—
CH_4	—	—	—	Cu_1, Cu_2	Zn_1, Zn_2, Zn_3, Zn_4, Zn_5, Zn_6, Zn_7, Zn_8, Zn_9, Zn_{10}

Fig. 3 Matrix showing which metal clusters stably adsorb which C_1 fragment (C, CH, CH_2, CH_3, and CH_4). Each C_1 fragment is shown in the leftmost column and each metal species is shown in the uppermost row. For example, in the C row, metal clusters that have been found to stably adsorb C are listed for each metal species. "—" denotes indicates that the corresponding metal cluster has not been found.

Please do not adjust margins

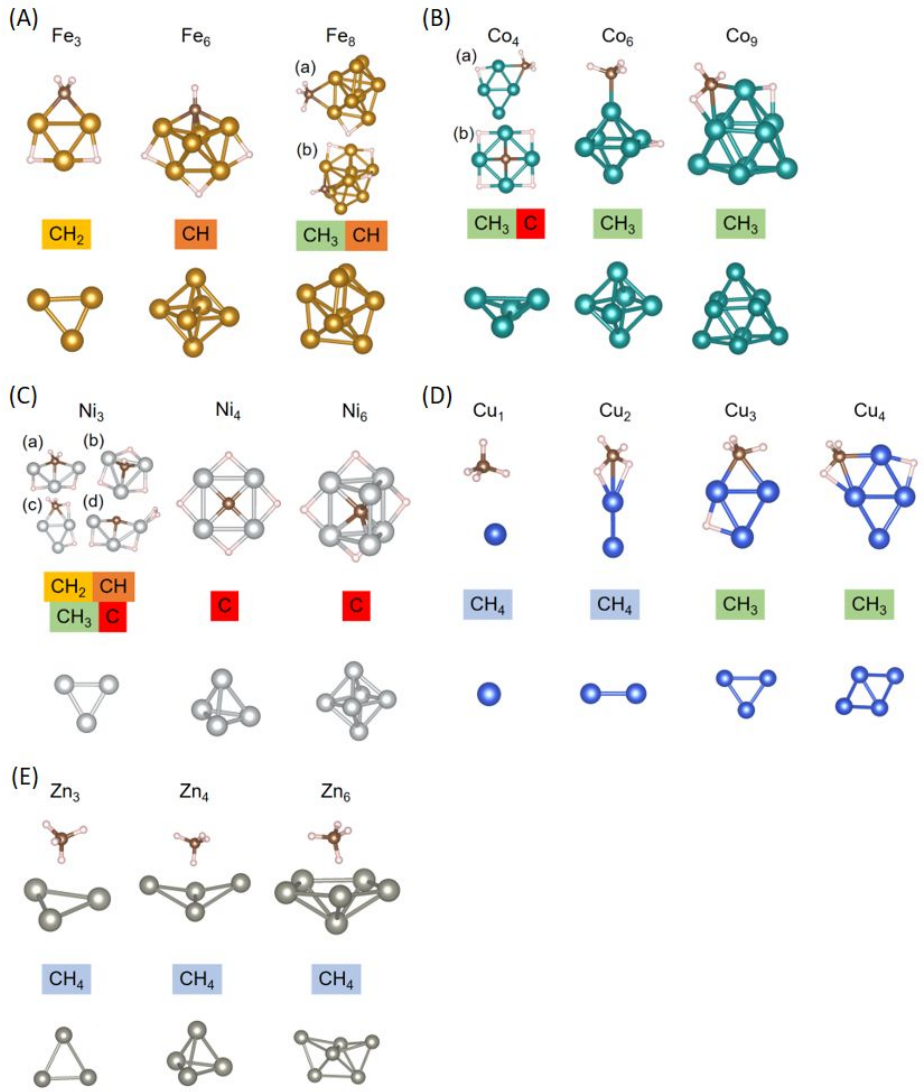

Fig. 4 Some of the most stable and metastable M_nCH_4 (M = Fe (A), Co (B), Ni (C), Cu (D), and Zn (E)) structures obtained from our CALYPSO calculations are shown. If a metastable structure exists, the structures are labelled (a), (b), (c) and (d), where (a) indicates the most stable structure while (b), (c), and (d) indicate metastable structures in alphabetical order from the most stable to the least stable. Below each M_nCH_4 structure, the corresponding most stable M_n structure is shown. Fe-Fe, Co-Co, Ni-Ni, and Cu-Cu bonds are shown only when the bond length is 3.0 Å or less. Zn-Zn bonds are shown only when the Zn-Zn bond is 3.5 Å or less. Fe-C, Co-C, Ni-C, and Cu-C bonds are shown only when the bond length is 2.5 Å or less. Fe-H, Co-H, Ni-H, and Cu-H bonds are shown only when the bond length is 2.0 Å or less. Here only a few representative structures are selected and shown. All of the cluster structures from n = 1 to 10 are shown in ESI†.

The structures of the most stable and metastable M_nCH_4 clusters were obtained from the structure search for each metal and each value of n. Based on the state of the C atom in the optimized M_nCH_4 cluster, we summarize in Fig. 3 which metal clusters stably adsorb which C_1 fragment.[76] Some representative cluster structures are selected for each metal and shown in Fig. 4. Complete figures with all the structures explored are found in section 4 of ESI†. To give an idea of how long M-C bonds are, radial distribution functions (RDFs) for the M-C bonds are shown in section 6 of ESI†.

Comparing the structures of the metal nanoclusters adsorbing a C_1 fragment with those of the metal nanoclusters alone, we see that the structures can be roughly divided into two groups: one slightly distorted by the adsorption of a C_1 fragment and the other transformed by the incorporation of a C_1 fragment as part of the metal nanocluster. Fe_3, Co_6, Cu_3, and Cu_4 are examples of the former, while Fe_6 and Ni_n (n = 4-10) are examples of the latter.

The structure of metal nanoclusters varies with metal species. For example, in the Zn nanoclusters, the interatomic distance between nearest neighbour Zn atoms tends to be large (almost in the range from 2.6 to 3.2 Å) compared to that of the other metal nanoclusters, which is almost in the range from 2.2 to 2.6 Å. Cu nanoclusters appear to have a tendency to take on a planar structure when the number of metal atoms is small. The structures of Co_4 (b) in Fig. 4 (B) and Ni_4 in Fig. 4 (C) also have planar structures, which are known as planar tetracoordinate carbon molecules.[77-79]

Looking over all of the obtained structures, it is clear that hydrogen atoms tend to be adsorbed on bridge sites or three-fold hollow sites. In the case of Zn, hydrogen will not be adsorbed. Only in the case of Ni_3 (d) in Fig. 4 (C), it is not a hydrogen atom but a hydrogen molecule that is adsorbed on the metal nanocluster in a side-on type. This can also be viewed as two H's bonded to the C atom in Ni_3 (a) combining to form H_2. Metal nanoclusters of one, two,

This journal is © The Royal Society of Chemistry 20xx

Please do not adjust margins

or three metal atoms tend to adsorb less hydrogen atoms than those of four or more metal atoms. This is probably due to the fact that when the number of metal atoms is small, there are fewer bridge sites and hollow sites to adsorb hydrogen.

If the C_1 fragment takes a form of CH_4 in the optimized structure, it is physisorbed or has an agostic interaction with a metal nanocluster.[80,81] In the case of the agostic interaction, the M-C distance is closer than that in the case of physisorption. The presence of the agostic interaction can be seen only in the case of Cu_2.

Depending on the form of the C_1 fragment, one can see a variety of adsorption behaviours: CH_3 is adsorbed on an on-top site or a bridge site, CH_2 on a bridge site or a three-fold hollow site, CH on a three- or four-fold hollow site, and C on a three-, four-, or five-fold hollow site or is even incorporated into the inside of the metal nanocluster. When the C atom is incorporated into the metal nanocluster, the coordination number of C is 6 or 7. It is evident that the less the number of H atoms in the C_1 fragment, the more bonds between the C_1 fragment and metal atoms are formed, a similar trend has been reported for its adsorption on metal surfaces.[82]

Fe and Co nanoclusters seem to have a tendency to stabilize adsorbed species of CH and CH_3. As the number of metal atoms in the nanocluster increases, CH becomes more stably adsorbed.

The Ni nanoclusters get to stabilize the adsorbed species of C as the number of atoms in the nanocluster increases. That C gets incorporated into the inside of the metal nanocluster or adsorbed at a five-fold hollow site on the cluster surface is found for the case of Ni.

In the Cu nanoclusters, the adsorbed species of CH_3 appears to tend to be stabilized almost exclusively, and the CH_3 species is often adsorbed on a bridge site.

When the number of metal atoms is small, various adsorbed species tend to be stabilized, but when the number increases, the adsorption of only one specific C_1 fragment seems to be selectively stabilized. For example, in the case of Ni, it is C, and in the case of Cu, it is CH_3. Therefore, the trend does not seem to change even if the number of metal atoms increases further.

In all the cases for the Zn nanoclusters, the C_1 fragment is stable in the form of CH_4, adsorbed on them in a physisorption manner, where the closest Zn-C distance is about 3.6 Å. Also, in the case of Cu_1 (see Fig. 4), the C_1 fragment is physisorbed in the form of CH_4, but the closest distance between the carbon atom and the metal atom is about 0.5 Å shorter than that in the cases of the Zn nanoclusters. The interaction between Zn and CH_4 can be predicted to be weaker than that between Cu and CH_4.

In closing this section, the above-mentioned results indicate that as may be often the case with metal clusters, the number of atoms and the type of elements that make up the metal nanoclusters can change which C_1 fragment is stabilized most on the cluster—there is a sweet spot here for engineering new catalysts.

b. Evaluation of the Methane Activation Capacity of Metal Nanoclusters

In order to discuss the methane activation capacity of each metal species based on the most stable structure and metastable structures obtained from the combination of CALYPSO and VASP calculations, we evaluated the methane activation capacity of metal M (M = Fe, Co, Ni, Cu, or Zn) using the following equation.

$$A_{\mathrm{M}} = \frac{1}{10}\sum_{n=1}^{10}\sum_{x=0}^{4}(4-x)P_{\mathrm{CH}_x}^{(n)}, \qquad (1)$$

where $P_{\mathrm{CH}_x}^{(n)}$ represents the probability of the presence of the C_1 fragment of CH_x (x = 1-4) on the nanocluster of M_n (n = 1-10). $P_{\mathrm{CH}_x}^{(n)}$ is calculated using the Boltzmann distribution as in the following equation.

$$P_{\mathrm{CH}_x}^{(n)} = \frac{\exp\left(-\frac{\Delta E_{\mathrm{CH}_x}^{(n)}}{kT}\right)}{\sum_{x=0}^{4}\exp\left(-\frac{\Delta E_{\mathrm{CH}_x}^{(n)}}{kT}\right)}, \qquad (2)$$

where $\Delta E_{\mathrm{CH}_x}^{(n)}$ is the relative energy of the M_n nanocluster adsorbing CH_x and $(4-x)$H compared to the most stable one. In this study, T is set to 300 K. If $\Delta E_{\mathrm{CH}_x}^{(n)}$ > 0.1 eV at this temperature, $\exp\left(-\frac{\Delta E_{\mathrm{CH}_x}^{(n)}}{kT}\right) \approx 0$, so $P_{\mathrm{CH}_x}^{(n)} \approx 0$. Thus, the structures with a relative energy of 0.1 eV or less affect the value of A_{M} significantly. Note that the effect of entropy is not taken into account here. To be accurate, $\Delta E_{\mathrm{CH}_x}^{(n)}$ should be replaced by the free energy difference, which we have not calculated to save computational resources. We discuss the effect of entropy in section 7 of ESI†, showing that the effect is not so large unless the temperature is high.

In eq. 1, $\sum_{x=0}^{4}(4-x)P_{\mathrm{CH}_x}^{(n)}$ represents the expected value of the number of H atoms adsorbed on the nanocluster of M_n apart from the C_1 fragment. The value obtained by averaging this value from n = 1 to n = 10 corresponds to A_{M}. Therefore, we can assume that the larger the value of A_{M}, the more H atoms are likely to be abstracted form methane when it interacts with a nanocluster of metal M. Metal nanoclusters with a larger value of A_{M} can be considered to have a higher methane activation capacity and have a higher probability of making methane over-oxidized.

A word of caution is necessary in understanding what A_{M} means. In eq. 2, $\Delta E_{\mathrm{CH}_x}^{(n)}$ can be viewed as the energy difference between the reaction intermediates pertinent to methane dehydrogenation. The kinetics of catalytic reactions is generally determined by the transition states, not the intermediates and products. Thermodynamics and kinetics are two different things. However, the Bell–Evans–Polanyi principle[83,84] links the two and shows that, in general, the relative rates of two reactions are related to which is thermodynamically more favourable.[85] Therefore, in this paper, we will focus on the thermodynamic stability of the reaction intermediates.

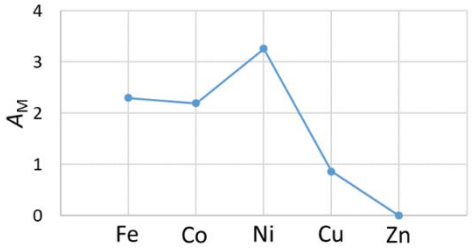

Fig. 5 Methane activation capacity A_{M} evaluated for the Fe, Co, Ni, Cu, and Zn nanoclusters (see the text for the definition of A_{M}).

The methane activation capacity of each metal species is shown in Fig. 5, which shows that the methane activation capacity decreases in the order of Ni > Fe > Co > Cu > Zn. Some might say that this would

be because the stronger the metal's affinity for hydrogen, the more H atoms are adsorbed on the metal nanocluster, resulting in the formation of a C_1 fragment with fewer H atoms thereon. However, as we will see later, things will prove not to be simple.

The methane activation capacity of the Cu nanoclusters is 0.86. It follows from this that the stable adsorption of CH_3 is favoured, indicating that the Cu nanoclusters may prevent the over-oxidation of methane and thus could find an application as a direct methane conversion catalyst.

The methane activation capacities of the Fe and the Co nanoclusters are 2.30 and 2.19, respectively. Although they appear to be able to produce ethylene through C-C coupling, as Fig. 3 and Fig. 4 show that the Co and the Fe nanoclusters are stable adsorbers of CH and CH_3, they are not expected to be applied to ethylene formation catalysts. However, for example, Fe_8, Co_4, Co_6, and Co_9 are stable adsorbers of CH_3, so their application as ethane formation catalysts could be promising.

Ni has the methane activation capacity of 3.26, which is too high. When the number of Ni atoms in the Ni nanocluster is 4 or larger, as Fig. 3 shows, the Ni nanoclusters will deprive methane of all of the H atoms. By contrast, Zn has the methane activation capacity of 0 and does not activate methane at all, making it unlikely to be used as a catalyst.

As reported in the literature,[24] the adsorption state of CH_4 on the Cu (111) surface is the most stable in the dehydrogenation of methane thereon. Note that the adsorption state of CH_3 on the Cu surface is less stable than that of CH_4. Therefore, it can be said that by changing the Cu solid to the Cu nanocluster, the activity of Cu is enhanced and the adsorbed state of CH_3 gets more stable than that of CH_4. Were the activity of the Cu nanoclusters not increased by nanoclustering, the most stable state of the C_1 fragment on the Cu nanoclusters would be CH_4, like the cases of the Zn nanoclusters. These findings clearly demonstrate the significance of using nanoclusters as a catalyst rather than solid surfaces.

The graph in Fig. 5 looks like a volcano-type plot, but things are not so simple because Fe has a slightly higher methane activation capacity than Co. This figure begs for a detailed explanation.

c. Detailed Electronic Structure Analysis

In this section, we will discuss the results of the calculations of the Fermi level, the DOS, the Bader charge, and the ICOHP to examine in more detail how the methane activation capacity of the metal nanoclusters varies depending on the metal species.

Let us begin with the Fermi level. Fig. 6 shows the Fermi levels of the Fe_{10}, Co_{10}, Ni_{10}, Cu_{10}, and Zn_{10} nanoclusters calculated with respect to the vacuum level. This figure shows that the Fermi level decreases in the order of $Fe_{10} > Co_{10} > Cu_{10} > Ni_{10} > Zn_{10}$.

The C_1 fragments, with the exception of CH_4, are a radical when placed in the gas phase if they do not interact with anything else. Here we are assuming a virtual state before any bond is formed between each C_1 fragment and each metal nanocluster. The radical nature of the C_1 fragments is associated with the presence of a singly occupied molecular orbital (SOMO). When an ionic bond is formed between them, charge transfer occurs from the metal nanocluster to the C_1 fragment's SOMO(s).[86]

The higher the Fermi level of a metal nanocluster, the larger the energy difference between the Fermi level and the SOMO(s) of the

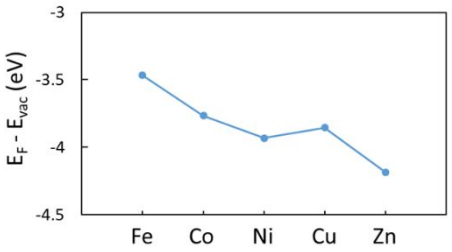

Fig. 6 Fermi levels of the Fe_{10}, Co_{10}, Ni_{10}, Cu_{10}, and Zn_{10} nanoclusters free from any C_1 fragment are calculated with respect to the vacuum level. E_F and E_{vac} denote the Fermi level and the vacuum level, respectively.

C_1 fragments (adsorbed species), which is schematically represented in Fig. S15 in ESI†. This should make it easier for an electron of the metal nanocluster to flow toward the adsorbed species' side. This is likely to be driven by a large stabilization energy due to charge transfer. A large charge difference between the surface of the metal nanocluster and the adsorbed species should ensue, leading to a stronger ionic bond between them. On the other hand, when the Fermi level is low and energetically close to the SOMO, the ionic bond will be weakened but this may be compensated by the growth of the covalent nature of the bond.

We would like to mention that the attempt to qualitatively understand the strength of a metal-C_1 fragment ionic bond based on the charge transfer model was initiated by Hoffmann and co-workers.[82] While they examined solid metal surfaces, we have applied their concepts to clustered metal surfaces in this paper.

When it comes to the strength of the covalent bonding between a C_1 fragment and a metal nanocluster, the so-called d-band centre model developed by Nørskov and co-workers is of significant help (see Fig. S16 in ESI† for its conceptual drawing).[87] The lower the energy level of the metal d-band, the more stabilized the bonding orbitals formed between the C_1 fragment and the metal surface and the stronger the covalent bond between them. On the other hand, as the number of electrons occupying the d-band increases, more and more electrons tend to enter the antibonding orbitals of the bond, and so the bond gets weaker. The application of the d-band model to the interaction of the C_1 fragments with the metal nanoclusters would be straightforward.

The Fermi levels of the Fe and Co nanoclusters are high, which makes them have higher ionicity in the Fe-C and Co-C bonds, whereas the Ni and Cu nanoclusters have low Fermi levels, which makes them have higher covalency in the Ni-C and Cu-C bonds. Since the Cu nanocluster has more d-electrons than the Ni nanocluster with the same number of metal atoms, when it interacts with a C_1 fragment, the number of electrons entering the antibonding orbitals of the Cu-C bond is expected to be larger than that of the Ni-C bond. Therefore, the Cu nanoclusters are predicted to have a moderate methane activation capacity due to their weaker affinity for carbon.

By looking at the results of the calculation of Bader charges, the strength of ionic bonds can be assessed. Fig. 7 shows the average Bader charges of the C_1 fragments (except for CH_4) adsorbed on the Fe, Co, Ni, and Cu nanoclusters. We will discuss only these four

This journal is © The Royal Society of Chemistry 20xx

Please do not adjust margins

clusters in the following because any stable structure of Zn nanoclusters adsorbing CH_x (x = 0-3) has not been obtained.

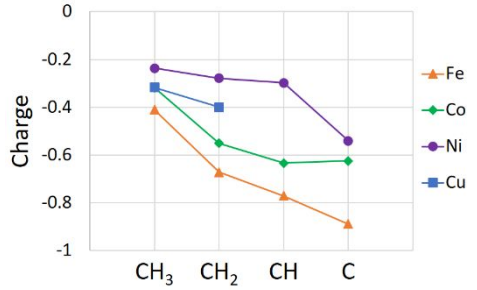

Fig. 7 The average value of the Bader charge calculated for each C_1 fragment, CH_x (x = 0-3), adsorbed on each metal nanocluster is plotted, where the Bader charge for the entire C_1 fragment including the H atoms was taken into account. As for Cu, we have not obtained any stable adsorption structure of CH and C, so the average value for them is absent. For the average calculation, all the stable and metastable structures obtained from our CALYPSO calculations were taken into account.

Fig. 7 shows that the magnitude of the negative charge of the C_1 fragment decreases in the order of Fe > Co > Cu > Ni, indicating that the ionicity of the M-C bond decreases in this order. This order is consistent with the decreasing order of the Fermi levels of the nanoclusters shown in Fig. 6.

From Fig. 7, it can also be seen that the magnitude of the negative charge of the C_1 fragment increases as the number of the H atoms bonding to it decreases, indicating that the less the H atoms in the C_1 fragment, the greater the ionic bonding nature of the interaction between the C_1 fragment and the nanocluster. This is because the less H atoms in the C_1 fragment, the more metal atoms tend to be coordinated to the C_1 fragment and the more electrons are transferred from the metal nanocluster to the C_1 fragment.

Fig. 8 shows the average Bader charges of adsorbed H atoms on each of the Fe, Co, Ni, and Cu nanoclusters. Note that we have not obtained any stable structure of Zn nanoclusters adsorbing H. As shown in this figure, the magnitude of the negative charge of H decreases in the order of Fe > Co > Ni > Cu, and so the ionicity of the M-H bond decreases in the same order.

Based on the Bader charge, the strength of ionic bonds can nicely

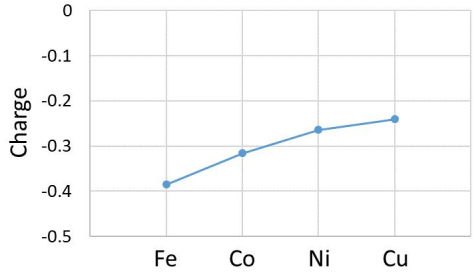

Fig. 8 The average value of the Bader charge per H atom adsorbed on each metal nanocluster is plotted. For the average calculation, all the stable and metastable structures obtained from our CALYPSO calculations were taken into account.

be evaluated, but the strength of covalent bonds cannot. Therefore, we calculated the COHP, a measure that allows one to assess the strength of the covalent bond between two atoms. The COHP results from multiplying the DOS by the overlap population of the bond weighted by the Hamiltonian matrix elements associated with the bond.[72,73] Negative and positive COHP values are indicative of stabilizing (bonding) and destabilizing (antibonding) covalent interactions, respectively.[88,89] The ICOHP value is obtained from the integration of the COHP up to the Fermi level. The larger the magnitude of the negative value of the ICOHP, the stronger the corresponding covalent bond is.[90,91]

Fig. 9a shows average ICOHP values calculated for the interaction between the C_1 fragments and the metal nanoclusters, where the M-C bonds between each of the Fe, Co, Ni, and Cu nanoclusters and each of the C_1 fragments were taken into account. This figure shows that the less the H atoms in the C_1 fragment, the stronger the covalent bonding nature of the M-C bond. Also, by and large, the strength of the M-C covalent bonding nature was found to decrease in the order of Ni > Co ≈ Fe > Cu. This order is in good agreement with that of A_M, suggesting that the covalent nature of the M-C bond has a significant effect on the activity of the metal clusters.

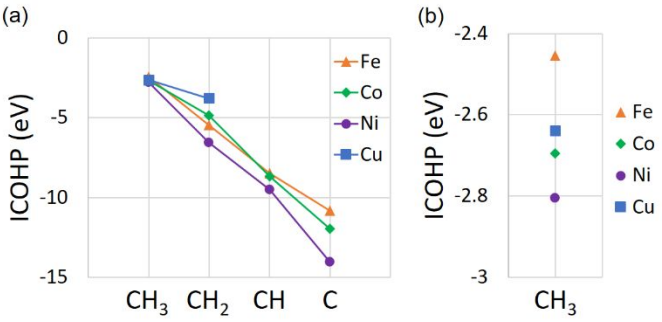

Fig. 9 (a) For each C_1 fragment, CH_x (x = 0-3), the average of the sum of the ICOHP values calculated for the M-C bonds less than 2.5 Å length on each of the Fe, Co, Ni, and Cu nanoclusters is plotted. As for Cu, we have not obtained any stable adsorption structure of CH and C, so the average value for them is absent. (b) An expanded view of the graph showing the average ICOHP values for the M-CH_3 bonds.

In the case of Cu, the absolute values of the ICOHP are smaller than those calculated for the cases of the other nanoclusters. This may be due to more electrons pushed into the antibonding orbitals formed between the C_1 fragment and the surface of the Cu nanoclusters. The results mentioned above are consistent with the trend observed in the methane activation capacity of each metal nanocluster shown in Fig. 5.

On the scale of Fig. 9a, the values of the ICOHP for the M-CH_3 bonds appear to be almost the same for all the metal species, but that is not true. As shown in Fig. 9b, a scaled-up version, the strength of the covalent M-CH_3 bond decreases in the order of Ni > Co > Cu > Fe. The strong covalent nature of the Ni-CH_x bonds is a common trend found regardless of the number of the H atoms in the C_1 fragment. This is also consistent with the fact that the Ni-C RDF peak is located at the shortest distance with the largest intensity (see Fig. S14 in ESI†).

According to scaling relations, which are linear relationships between adsorption energies of similar adsorbates, as the number of H's in CH_x decreases, the strength of the covalent bond formed between the C_1 fragment and a metal surface becomes larger.[92,93] As the C_1 fragment gets deprived of more and more H atoms by a metal surface, it gets more strongly bound to the surface, reflecting reinforced stabilization of the C_1 by the surface; hence, one might tend to fall into the paradox that methane dehydrogenation (over-oxidation) would easily proceed on any metal surface. However, one needs to remind oneself of the fact that the C_1 becomes more and more destabilized as dehydrogenation progresses (see Fig. S1 in ESI†). Thus, the extent to which the methane dehydrogenation

reaction proceeds, i.e., which CH_x species is most stabilized on the surface, depends on the delicate balance between CH_x destabilization due to C-H bond cleavage and CH_x stabilization due to M-C bond formation.

Fig. 10 shows the average ICOHP value per hydrogen atom calculated for the bonds between the hydrogen atoms not belonging to the C_1 fragment and the metal atoms of each Fe, Co, Ni, and Cu nanocluster. This figure shows that the absolute value of the ICOHP in the case of Cu is small and so the covalent nature of the Cu-H bond is weak. Similar to the case of the Cu-C bond, this may also be due to the presence of more electrons in the antibonding orbitals of the Cu-H bond.

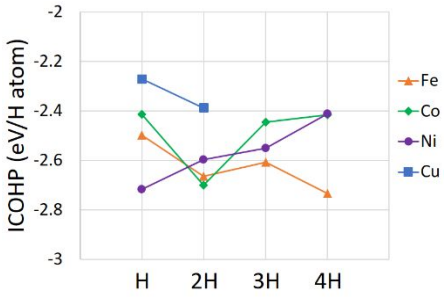

Fig. 10 For each C_1 fragment, CH_x (x = 0-3), the average of the sum of the ICOHP values calculated for the M-H bonds of less than 2.0 Å length on each of the Fe, Co, Ni, and Cu nanoclusters is divided by the number of the adsorbed H atoms. The ICOHP value thus calculated is plotted as a function of the number of the adsorbed H atoms. As for Cu, we have not obtained any stable structure on which three or four H atoms are adsorbed, so average values for 3H and 4H are absent.

For the cases of Fe, Co, and Ni, the absolute values of the ICOHP vary in a similar range of values. This indicates that on the whole, the covalent-bond strengths of the Fe-H, Co-H, and Ni-H bonds are about the same. The covalent-bond strength of the M-H bond may be of the following order: Fe ≈ Co ≈ Ni > Cu. This suggests that the reason for the markedly high methane activation capacity of Ni compared to Fe and Co may not be due to the high affinity of Ni for H, rather due to that of Ni for C. It should be noted that the M-H ICOHP value can be regarded as an indicator of the hydrogen affinity to the metal surface and has been reported to be a good descriptor for the reactivity of catalysts toward methane only in the case of the homolytic C-H cleavage mechanism involving the formation of a CH_3 radical.[94,95] In other words, not everything can be explained by the affinity between metal and hydrogen alone.

As far as the case where only one H atom is adsorbed goes, the covalent-bond strength of the M-H bond decreases in the order of Ni > Fe > Co > Cu. It would be of interest to note that in the literature, there is a study of the adsorption energy of H on polycrystalline transition metal surfaces, reporting that the magnitude of the adsorption energy decreases in the order of Ni > Fe > Co > Cu.[96]

From the Bader charge discussed so far, it has been found that the ionic bond strengths of the M-C and M-H bonds decrease in the orders of Fe > Co > Cu > Ni and Fe > Co > Ni > Cu, respectively. The ICOHP values show that the covalent-bond strengths for the M-C and M-H interactions decrease in the orders of Ni > Co ≈ Fe > Cu and Fe ≈ Co ≈ Ni > Cu, respectively. In summary, the bonding of the adsorbed species to Fe and that to Co are highly ionic, while that to Ni is highly covalent. On the other hand, both ionic and covalent bonds between Cu and the adsorbed species are weak.

The ionic-bond strength of the M-C and M-H bonds can be qualitatively understood on the basis of the height of the Fermi level (or the magnitude of the work function) of each metal nanocluster. The covalent-bond strengths of the M-C and M-H bonds can quantitatively be measured by using the ICOHP. To qualitatively understand the covalency, we have analysed the DOS of the metal nanoclusters and the adsorbed species.

The detailed analysis of the DOS is presented in section 9 of ESI.† Here, we would like to address it only briefly. From the calculated DOS plots, we see that the d-band centre becomes lower in the order of Fe > Co > Ni > Cu > Zn. The SOMO of CH_3, the main component of which is the $2p_z$ orbital of the C atom, may be considered as a representative orbital of the C_1 fragment, responsible for its bonding to the surface.[82] The smallest energy gap between the d-band centre and the $2p_z$ orbital is achieved for Ni, which may be deemed the origin of the strongest covalent nature of the bonding of Ni to the C_1 fragment of the nanoclusters investigated.

We have evaluated the covalent and ionic bonding characters of the M-C and M-H bonds, and the qualitative agreement between the covalent strength of the M-C bond shown in Fig. 9 and the magnitude of A_M indicates that the covalent nature of the M-C bond is an important factor controlling the activity of the metal cluster. Since the covalent strength of the Fe-C and Co-C bonds is almost the same, the difference in the ionic bond strength affects the value of A_M. The strength of ionic bonds to the adsorbed species of Fe is higher than that of Co. This would be why Fe has a larger A_M value than Co. The weak methane activation ability of Cu compared to Fe, Co, and Ni may be due to the fact that both covalent and ionic interactions of Cu with the adsorbed species are reasonably weak. This is also consistent with the fact that the Cu-C RDF peak is located at the longest distance with the smallest intensity (see Fig. S14 in ESI†). The reason why Zn does not activate methane at all may be that Zn and the adsorbed species can form neither ionic nor covalent bonding.

The activity of the Ni nanoclusters seems too strong to be used as a catalyst for the direct conversion of methane due to the problem of over-oxidation. On the contrary, the Cu nanoclusters may well be suitable for catalyzing the direct conversion of methane via C-C coupling reaction because of their moderate activity and the unique ability to stabilize CH_3 as the adsorbed species. This idea, however, should be taken with caution because when CH_3 is too stabilized, then it would require a high activation energy to detach it and then form the C-C bond. Nevertheless, looking at the ICOHP values for Cu-C bonds, we would not say that CH_3 is too stabilized on Cu nanoclusters. Therefore, Cu nanoclusters are promising catalyst candidates. It is worth noting that Varghese and Mushrifthe[41] theoretically showed that on small Cu clusters, coupling reactions of CH_x (x = 1–3) species have energy barriers significantly lower than complete dehydrogenation of methane to carbon.

In this paper, we have investigated naked metal nanoclusters; however, we are aware that neutral clusters of transition metals synthesized are actually not naked but stabilized by the coordination of ligands or surfactants.[97] Here it would be of interest to note that Cavell and co-workers synthesized a ligand-supported Cu_6 cluster adsorbing two CH_3 groups, finding it very stable in the solid state under an inert atmosphere at room temperature.[98]

This journal is © The Royal Society of Chemistry 20xx

Please do not adjust margins

IV. Conclusions

In search of a potential candidate of catalysts for the direct methane conversion, we have performed a theoretical study using particle swarm optimization combined with density functional theory calculations on Fe, Co, Ni, Cu, and Zn nanoclusters, revealing how the type of C_1 fragments (CH_4, CH_3, CH_2, CH, and C) stabilized by the metal nanoclusters varies with the metal species and the number of metal atoms in the nanocluster.

Based on the optimized nanocluster structures adsorbing a C_1 fragment in its most stable form, we have proposed a way to estimate the methane activation capacity of each metal, which has been found to decrease in the order of Ni > Fe > Co > Cu > Zn. The highest methane activation capacity of Ni is considered to come from the strongest covalent nature of the interaction of Ni with the adsorbed C_1 species according to the COHP analysis. The Bader charge analysis shows that the ionic bonding of each C_1 fragment to Fe is stronger than that to Co, while their covalent bond strengths are almost comparable according to the COHP analysis. This would be the reason why Fe has a higher methane activation capacity than Co. The weak methane activation ability of Cu compared to Fe, Co, and Ni should derive from the fact that both covalent and ionic bonds of Cu to the adsorbed species are reasonably weak. That Zn does not activate methane at all may be because Zn and any C_1 fragment tend to form neither ionic nor covalent bonding. The above findings are nicely corroborated by the results for the analyses of the Fermi level, the Bader charge, the crystal orbital Hamilton population, and the density of states.

A close examination of the results indicates that the Fe, Co, and Ni nanoclusters are likely to over-oxidize methane, while the Zn nanoclusters may not be able to activate methane, so their application to catalysts for the direct methane conversion and methane partial oxidation is unlikely. Since we have found that the Cu nanoclusters do not adsorb C and CH as a stable species but do adsorb CH_3 stably, the Cu nanoclusters may well be used as a catalyst for the direct conversion of methane to ethane via a C-C coupling reaction. It is notable that these properties of the Cu nanoclusters are unique to the nanocluster, not found on the Cu (111) surface. Many things remain to be done to bridge the gap between this fundamental research and the practical application of the metal nanoclusters to a catalyst; for example, whether the clusters can maintain their shape in the operating environment of a catalytic reaction, but this paper is reasonably long so that we would like to leave them for the future research.

Conflicts of interest

There are no conflicts to declare.

Acknowledgements

This work was supported by KAKENHI grants (numbers JP17K14440, JP17H03117, and JP21K04996) from the Japan Society for the Promotion of Science (JSPS) and the Ministry of Education, Culture, Sports, Science and Technology of Japan (MEXT) through the MEXT projects Integrated Research Consortium on Chemical Sciences, Cooperative Research Program of Network Joint Research Center for Materials and Devices and Elements Strategy Initiative to Form Core Research Center, and by JST-CREST JPMJCR15P5 and JST-Mirai JPMJMI18A2. The computations in this work were primarily performed using the computer facilities at the Research Institute for Information Technology, Kyushu University. Y.T. is grateful for a JSPS Grant-in-Aid for Scientific Research on Innovative Areas (Discrete Geometric Analysis for Materials Design, grant numbers JP18H04488 and JP20H04643, and Mixed Anion, grant number JP19H04700).

Notes and references

1 J. R. Rostrup-Nielsen, *Catal. Sci. Technol.*, 1984, **5**, 1–117.
2 J. R. Rostrup-Nielsen, *J. Catal.*, 1984, **85**, 31–43.
3 Y. Matsumura and T. Nakamori, *Appl. Catal. A Gen.*, 2004, **258**, 107–114.
4 S. Uemiya, N. Sato, H. Ando, T. Matsuda and E. Kikuchi, *Appl. Catal.*, 1990, **67**, 223–230.
5 J. Gao, Z. Hou, J. Guo, Y. Zhu and X. Zheng, *Catal. Today*, 2008, **131**, 278–284.
6 S. Rakass, H. Oudghiri-Hassani, P. Rowntree and N. Abatzoglou, *J. Power Sources*, 2006, **158**, 485–496.
7 P. O. Sharma, S. Swami, S. Goud and M. A. Abraham, *Environ. Prog.*, 2008, **27**, 22–29.
8 K. Otsuka and Y. Wang, *Appl. Catal. A Gen.*, 2001, **222**, 145–161.
9 W. Cho, S. H. Lee, W. S. Ju, Y. Baek and J. K. Lee, *Catal. Today*, 2004, **98**, 633–638.
10 K. O. Christensen, D. Chen, R. Lødeng and A. Holmen, *Appl. Catal. A Gen.*, 2006, **314**, 9–22.
11 J. R. Rostrup-Nielsen and I. Alstrup, *Catal. Today*, 1999, **53**, 311–316.
12 J. De Deken, P. G. Menon, G. F. Froment and G. Haemers, *J. Catal.*, 1981, **70**, 225–229.
13 D. L. Trimm, *Catal. Today*, 1997, **37**, 233–238.
14 C. J. Liu, J. Ye, J. Jiang and Y. Pan, *ChemCatChem*, 2011, **3**, 529–541.
15 K. Yoshizawa, *Direct Hydroxylation of Methane*, Springer Singapore, 2020.
16 D. W. Blaylock, T. Ogura, H. G. William and J. O. B. Gregory, *J. Phys. Chem. C*, 2009, **113**, 4898–4908.
17 T. Kamachi, M. Saito, Y. Tsuji and K. Yoshizawa, *J. Comput. Chem. Japan*, 2017, **16**, 147–148.
18 Y. Matsumura, J. B. Moffat, S. Sugiyama, H. Hayashi, N. Shigemoto and K. Saitoh, *J. Chem. Soc. Faraday Trans.*, 1994, **90**, 2133–2140.
19 Y. Matsumura, S. Sugiyama, H. Hayashi and J. B. Moffat, *J. Solid State Chem.*, 1995, **114**, 138–145.
20 Q. T. Trinh, A. Banerjee, Y. Yang and S. H. Mushrif, *J. Phys. Chem. C*, 2017, **121**, 1099–1112.
21 T. L. M. Pham, E. G. Leggesse and J. C. Jiang, *Catal. Sci. Technol.*, 2015, **5**, 4064–4071.
22 T. Toyao, K. Suzuki, S. Kikuchi, S. Takakusagi, K.-I. Shimizu and I. Takigawa, *J. Phys. Chem. C*, 2018, **122**, 8315–8326.
23 X. Hao, Q. Wang, D. Li, R. Zhang and B. Wang, *RSC Adv.*, 2014, **4**, 43004–43011.
24 G. Gajewski and C. W. Pao, *J. Chem. Phys.*, 2011, **135**, 064707.
25 J. Niu, J. Ran, X. Du, W. Qi, P. Zhang and L. Yang, *Mol. Catal.*, 2017, **434**, 206–218.
26 H. S. Bengaard, J. K. Nørskov, J. Sehested, B. S. Clausen, L. P. Nielsen, A. M. Molenbroek and J. R. Rostrup-Nielsen, *J. Catal.*, 2002, **209**, 365–384.

This journal is © The Royal Society of Chemistry 20xx

Please do not adjust margins

27 R. L. Arevalo, S. M. Aspera, M. C. S. Escaño, H. Nakanishi and H. Kasai, *Sci. Rep.*, 2017, **7**, 13963.
28 J. A. Widegren and R. G. Finke, *J. Mol. Catal. A Chem.*, 2003, **191**, 187–207.
29 M. B. Thathagar, J. Beckers and G. Rothenberg, *J. Am. Chem. Soc.*, 2002, **124**, 11858–11859.
30 X. L. Ma, J. C. Liu, H. Xiao and J. Li, *J. Am. Chem. Soc.*, 2018, **140**, 46–49.
31 Z. Luo, A. W. Castleman and S. N. Khanna, *Chem. Rev.*, 2016, **116**, 14456–14492.
32 J. D. Aiken, Y. Lin and R. G. Finke, *J. Mol. Catal. A Chem.*, 1996, **114**, 29–51.
33 N. Toshima, *Pure Appl. Chem.*, 2000, **72**, 317–325.
34 E. C. Tyo and S. Vajda, *Nat. Nanotechnol.*, 2015, **10**, 577–588.
35 H. Seenivasan and A. K. Tiwari, *Comput. Theor. Chem.*, 2015, **1064**, 7–14.
36 R. K. Singha, Y. Tsuji, M. H. Mahyuddin and K. Yoshizawa, *J. Phys. Chem. C*, 2019, **123**, 9788–9798.
37 Z. Cheng, N. A. Fine and C. S. Lo, *Top. Catal.*, 2012, **55**, 345–352.
38 Z. Cheng and C. S. Lo, *Ind. Eng. Chem. Res.*, 2013, **52**, 15447–15454.
39 J. Y. Damte, Z. Zhu, P. Lin, C. Yeh and J. Jiang, *J. Comput. Chem.*, 2020, **41**, 194–202.
40 T. S. Khan, S. Balyan, S. Mishra, K. K. Pant and M. A. Haider, *J. Phys. Chem. C*, 2018, **122**, 11754–11764.
41 J. J. Varghese and S. H. Mushrif, *J. Chem. Phys.*, 2015, **142**, 184308.
42 J. Wei and E. Iglesia, *J. Phys. Chem. B*, 2004, **108**, 4094–4103.
43 J. Wei and E. Iglesia, *Angew. Chem. Int. Ed.*, 2004, **43**, 3685–3688.
44 T. Li, S. J. Wang, C. S. Yu, Y. C. Ma, K. L. Li and L. W. Lin, *Appl. Catal. A Gen.*, 2011, **398**, 150–154.
45 Y. Hou, S. Ogasawara, A. Fukuoka and H. Kobayashi, *Catal. Sci. Technol.*, 2017, **7**, 6132–6139.
46 Y. Wang, J. Lv, L. Zhu and Y. Ma, *Phys. Rev. B - Condens. Matter Mater. Phys.*, 2010, **82**, 094116.
47 Y. Wang, J. Lv, L. Zhu and Y. Ma, *Comput. Phys. Commun.*, 2012, **183**, 2063–2070.
48 B. Gao, P. Gao, S. Lu, J. Lv, Y. Wang and Y. Ma, *Sci. Bull.*, 2019, **64**, 301–309.
49 R. Eberhart and J. Kennedy, in *Proceedings of the International Symposium on Micro Machine and Human Science*, IEEE, 1995, pp. 39–43.
50 S. Kiranyaz, T. Ince and M. Gabbouj, *Adapt. Learn. Optim.*, 2014, **15**, 45–82.
51 S. T. Call, D. Y. Zubarev and A. I. Boldyrev, *J. Comput. Chem.*, 2007, **28**, 1177–1186.
52 G. Kresse and J. Furthmüller, *Phys. Rev. B - Condens. Matter Mater. Phys.*, 1996, **54**, 11169–11186.
53 G. Kresse and J. Hafner, *Phys. Rev. B*, 1993, **47**, 558–561.
54 G. Kresse and J. Hafner, *Phys. Rev. B*, 1994, **49**, 14251–14269.
55 G. Kresse and J. Furthmüller, *Comput. Mater. Sci.*, 1996, **6**, 15–50.
56 C. Blum and X. Li, in *Swarm Intelligence*, Springer Berlin Heidelberg, 2008, pp. 43–85.
57 E. Zurek, *Rev. Comput. Chem.*, 2016, **29**, 274–326.
58 P. Lv, Z. Lu, S. Li, D. Ma, W. Zhang, Y. Zhang and Z. Yang, *RSC Adv.*, 2016, **6**, 104388–104397.
59 X. Xia, X. Kuang, C. Lu, Y. Jin, X. Xing, G. Merino and A. Hermann, *J. Phys. Chem. A*, 2016, **120**, 7947–7954.
60 W. G. Sun, J. J. Wang, C. Lu, X. X. Xia, X. Y. Kuang and A. Hermann, *Inorg. Chem.*, 2017, **56**, 1241–1248.
61 Y. Tsuji, R. Hoffmann and J. S. Miller, *Polyhedron*, 2016, **103**, 141-149.
62 L. Zhao, J. G. Du and G. Jiang, *J. Alloys Compd.*, 2018, **745**, 497-504.
63 G. L. Gutsev and C. W. Bauschlicher, *J. Phys. Chem. A*, 2003, **107**, 4755-4767.
64 K. Momma and F. Izumi, *J. Appl. Crystallogr.*, 2011, **44**, 1272–1276.
65 J. P. Perdew, K. Burke and M. Ernzerhof, *Phys. Rev. Lett.*, 1996, **77**, 3865–3868.
66 P. E. Blöchl, *Phys. Rev. B*, 1994, **50**, 17953–17979.
67 G. Kresse and D. Joubert, *Phys. Rev. B - Condens. Matter Mater. Phys.*, 1999, **59**, 1758–1775.
68 S. Grimme, *J. Comput. Chem.*, 2006, **27**, 1787–1799.
69 Á. Szécsényi, G. Li, J. Gascon and E. A. Pidko, *ACS Catal.* 2018, **8**, 7961−7972.
70 Y. Wang, J. Lv, Q. Li, H. Wang and Y. Ma, in *Handbook of Materials Modeling*, Springer International Publishing, 2020, pp. 2729–2756.
71 R. F. W. Bader, *Chem. Rev.*, 1991, **91**, 893–928.
72 R. Dronskowski and P. E. Blöchl, *J. Phys. Chem.*, 1993, **97**, 8617–8624.
73 V. L. Deringer, A. L. Tchougréeff and R. Dronskowski, *J. Phys. Chem. A*, 2011, **115**, 5461–5466.
74 S. Maintz, V. L. Deringer, A. L. Tchougréeff and R. Dronskowski, *J. Comput. Chem.*, 2013, **34**, 2557–2567.
75 S. Maintz, V. L. Deringer, A. L. Tchougréeff and R. Dronskowski, *J. Comput. Chem.*, 2016, **37**, 1030–1035.
76 We found many structures in a narrow energy range, which structures are almost identical except for the position of adsorbed H. Therefore, it would be expected that H can easily move on the metal nanoclusters. We do not distinguish them as distinct structures but regard them as the same structure. Slightly distorted structures were also considered to be the same structure.
77 R. Hoffmann, R. W. Alder and C. F. Wilcox, *J. Am. Chem. Soc.*, 1970, **92**, 4992–4993.
78 S.-D. Li, G.-M. Ren, C.-Q. Miao and Z.-H. Jin, *Angew. Chem.* 2004, **116**, 1395–1397.
79 J. C. Guo, L. Y. Feng and X. Y. Zhang, *Comput. Theor. Chem.*, 2018, **1125**, 95–102.
80 M. Brookhart and M. L. H. Green, *J. Organomet. Chem.*, 1983, **250**, 395–408.
81 M. Brookhart, M. L. H. Green and G. Parkin, *Proc. Natl. Acad. Sci. U. S. A.*, 2007, **104**, 6908–6914.
82 C. Zheng, Y. Apeloig and R. Hoffmann, *J. Am. Chem. Soc.*, 1988, **110**, 749–774.
83 R. P. Bell, *Proc. R. Soc. London, Ser. A*, 1936, **154**, 414–429.
84 M. G. Evans and M. Polanyi, *Trans. Faraday Soc.*, 1936, **32**, 1333–1360.
85 W. T. Borden, R. Hoffmann, T. Stuyver and B. Chen, *J. Am. Chem. Soc.* 2017, **139**, 9010–9018.
86 Note that CH_3, CH_2, CH, and C have one, two, three, and four SOMOs, respectively. This is predicted from the number of unpaired electrons held by the C_1 fragment.
87 J. K. Nørskov, F. Abild-Pedersen, F. Studt and T. Bligaard, *Proc. Natl. Acad. Sci. U. S. A.*, 2011, **108**, 937–943.
88 M. Pokhrel, N. Dimakis, C. Dannangoda, S. K. Gupta, K. S. Martirosyan and Y. Mao, *Molecules*, 2020, **25**, 4847.
89 S. Steinberg and R. Dronskowski, *Crystals*, 2018, **8**, 225.
90 I. D. Aditya, D. Matsunaka, Y. Shibutani and S. Haryono, *Mater. Trans.*, 2018, **59**, 1684–1690.
91 X. J. Gu, S. J. Poon, G. J. Shiflet and M. Widom, *Appl. Phys. Lett.*, 2008, **92**, 161910.
92 F. Abild-Pedersen, J. Greeley, F. Studt, J. Rossmeisl, T. R. Munter, P. G. Moses, E. Skúlason, T. Bligaard and J. K. Nørskov, *Phys. Rev. Lett.*, 2007, **99**, 016105.
93 M. M. Montemore and J. W. Medlin, *Catal. Sci. Technol.*, 2014, **4**, 3748–3761.
94 A. A. Latimer, A. R. Kulkarni, H. Aljama, J. H. Montoya, J. S. Yoo, C. Tsai, F. Abild-Pedersen, F. Studt and J. K. Norskov, *Nat. Mater.*, 2017, **16**, 225–229.

This journal is © The Royal Society of Chemistry 20xx

Please do not adjust margins

95 C. Liu, G. Li and E. A. Pidko, *Small Methods* 2018, **2**, 1800266.
96 I. Toyoshima and G. A. Somorjai, *Catal. Rev.*, 1979, **19**, 105–159.
97 R. Hoffmann, *Angew. Chem. Int. Ed.*, 2013, **52**, 93–103.
98 G. Ma, M. J. Ferguson, R. McDonald and R. G. Cavell, *Organometallics*, 2010, **29**, 4251–4264.

This journal is © The Royal Society of Chemistry 20xx

Please do not adjust margins